Emission Spectroscopy Diagnosis of Arc-heated Plasma in Martian and Earth Atmosphere

Hui Zeng (zenghuikeda@outlook.com)
China Academy of Aerospace Aerodynamics
Dongbin Ou
China Academy of Aerospace Aerodynamics
Peng Wen
China Academy of Aerospace Aerodynamics
Xinying Zhu
China Academy of Aerospace Aerodynamics
Guoming Yang
China Academy of Aerospace Aerodynamics

Research Article

Keywords: linear plasma torch, cathode erosion, emission spectroscopy, temperature measurement, copper concentration

Posted Date: April 25th, 2022

DOI: https://doi.org/10.21203/rs.3.rs-1567300/v1

Emission Spectroscopy Diagnosis of Arc-heated Plasma in Martian and Earth Atmosphere

Hui Zeng*, Dongbin Ou, Peng Wen, Xinying Zhu, Guoming Yang

China Academy of Aerospace Aerodynamics, Beijing Key Laboratory of Arc Plasma Application Equipment，Beijing, China, 100074

*Corresponding author: zenghuikeda@outlook.com

Abstract: In-situ quantitative measurements are performed in a 300 kW DC magnetically-rotating linear plasma torch to investigate thermal characteristics of arc plasma and electrode erosion by utilizing optical emission spectroscopy. Time-resolved gas temperatures and mole fraction of copper concentrations are measured to evaluate the state of arc plasma and cathode erosion at different operation currents and magnetic fields. The erosion mass rates of the cathode by the OES method are in good accordance with the measurements by traditional weighing method over the operation range, demonstrating validity and accuracy for the developed OES method. The erosion rates of cathode for CO_2 plasma are lower than that for air plasma due to carbon element covering in the inner surface of the electrode by the SEM images. Detailed discussions of sensitivity and uncertainty by the OES method are given for air plasma and for CO_2 plasma.

Keywords: linear plasma torch; cathode erosion; emission spectroscopy; temperature measurement; copper concentration

1. Introduction

Arc-heated facilities provide a unique capability of simulating aero-thermodynamic environments for hypersonic vehicles entering through a planetary atmosphere and the facilities provide ground-based testing for thermal protection system (TPS) of reentry vehicle [1-3]. The plasma torch reproduces the aerodynamic heating conditions by generating an arc discharge between anode and cathode manufacturing by copper. The copper-electrodes erode by the arc spots and high temperature plasma flow during the electrical discharge[4], resulting in shortening of electrode life , premature electrode failure and threatening normal operation of the plasma torch

[5-7]. Moreover, the copper vapor evaporating from the electrodes and the constrictor disks will contaminate the plasma flow and copper contamination shows significant influence on the plasma thermos-physical properties, especially that of electrical conductivity, radiative emission coefficient and induced temperature drop for the plasma flow[8, 9]. Research in AEDC shows that copper contamination change the characteristics of plasma flow and the contaminated plasma flow is not suitable for microwave transmission testing[5]. The copper contamination has high catalytic effect on behavior and mechanism of carbon fiber reinforced silicon carbide (C/SiC) composites, including ablation and oxidation [10]. To study the electrode erosion, Guile[11] investigates the cathode erosion by considering factors such as spot size, velocity, current density, water flow and gas pressure and Zhukov[12] gives detailed discussion about the erosion of copper cold tubular electrodes by investigating the influence of magnetic field, rotation velocity, surface temperature of electrodes and different test medium. The electrode erosion remains a great challenge for the arc-heated facilities lacking of real-time quantitative measurements of copper contamination and evaluation of cathode erosion. Weighing electrode assemblies are regarded as a regular method to measure the mass fraction of copper in average, which is incapable for *in-situ* measurements. This average-value measurement method is disadvantageous to understand time-evolution of electrode erosion and a real-time diagnosis for copper concentration offer an opportunity for assessment of flow contamination.

Compared to the regular method as noted, optical methods provide great potential for non-intrusive, accurate, fast response and *in-situ* measurements and the emission and laser-based absorption spectroscopy diagnostics have been applied for quantitative measurements for real high-temperature and high speed flow in various ground test facilities[13, 14]. Especially with regard to plasma diagnostics in the arc-heated facilities, *Suhong Kim* presents quantitative optical measurements in the 60MW IHF segmented plasma wind tunnel located at NASA Ames and copper concentrations in the reservoir are measured by utilizing diode laser absorption spectroscopy(LAS) based on a selected copper line transition near 793.3nm[9]. *Stefan Lohle et al* in the Stuttgart university is committed to high enthalpy flow diagnostics and investigates gas-surface interaction by using emission spectroscopy and laser absorption spectroscopy in the plasma wind tunnel [15-17]. Emission spectroscopy measurements have been presented at the location of reservoir in

the arc-heated wind tunnel of China Academy of Aerospace Aerodynamics (CAAA) in previous works [18].

In this paper, optical emission spectroscopy(OES) is utilized to measure gas radiation of air plasma and CO_2 plasma in a developed 300kW DC magnetically-rotating linear plasma torch. Detailed analysis of spectral characteristics of the high-temperature flow in the cathode and downstream of anode are conducted for earth atmosphere and Martian atmosphere. A developed OES method is proposed for quantitative measurements of gas temperature and copper concentration and evaluating the state of arc plasma and cathode erosion at different operation currents and magnetic fields. The erosion rate of the cathode is analyzed by the OES method and the measured results by OES are compared with a traditional weighing method. Detailed discussions of sensitivity and uncertainty are given to assess measurement accuracy of the OES system.

2. Method

The radiation intensity of spectral transition of atomic species for the arc plasma ignoring stimulated transitions can be expressed as[19]

$$I = A_{ul} h_{ul} v_{ul} n_u \tag{1}$$

Where A_{ul} [s^{-1}] is Einstein coefficient, h_{ul} [Js] is plank constant, v_{ul} [cm^{-1}] is the center frequency of the atomic line, n_u [cm^{-3}] is particle density of upper energy state. "*u*" represents upper energy state and"*l*" represents lower energy state. Test gas is injected into the constrictor of the plasma torch and heated by the thermal arc discharge to high enthalpy plasma flow, which the flow velocity is low subsonic and the arc plasma in the reservoir upstream of the nozzle can be assumed to be in local thermochemical equilibrium(LTE) state and be considered as optically thin plasma by previous studies [19-23]. In thermal equilibrium, the populations of the excited states, n_u, are related to the total density of the species of concern, n_0, by a Maxwell-Boltzmann distribution:

$$n_u = n_0 \frac{g_u}{Q(T)} \exp(-\frac{E_u}{kT})$$
$$n_0 = \frac{PX}{kT} \tag{2}$$

Where n_0 [cm^{-3}] is the total particle density, g_u is degeneracy of the upper state, $Q(T)$ is partition function, k [JK^{-1}] is Boltzmann constant, E_u [cm^{-1}] is excited state energy for upper energy state, P[Mpa] and T[K] represent gas pressure and temperature in the reservoir. We can therefore give the relationship by comparing the spectral intensities of the selection lines for Cu I and O I:

$$\frac{I_{Cu}}{I_O} = \frac{X_{Cu}}{X_O} \frac{v_{0\_Cu}}{v_{0\_O}} \frac{A_{Cu}}{A_O} \frac{g_{u\_Cu}}{g_{u\_O}} \frac{Q_o}{Q_{Cu}} \exp(-\frac{E_{Cu} - E_O}{kT}) \tag{3}$$

The mole fraction of atomic copper can be expressed as follows:

$$X_{Cu} = \frac{I_{Cu}}{I_O} X_O (\frac{v_{0\_Cu}}{v_{0\_O}} \frac{A_{Cu}}{A_O} \frac{g_{u\_Cu}}{g_{u\_O}} \frac{Q_o}{Q_{Cu}} \exp(-\frac{E_{Cu} - E_O}{kT}))^{-1} \tag{4}$$

The Einstein coefficient A, upper state degeneracy g_u and central wavelength for the selected line transitions are presented in Table 1, and the partition function of atomic oxygen is modeled and described by Gianpiero Colonna and can be expressed by the following equation [24]. The partition function of copper can be obtained from NIST Atomic Spectra Database [25].

Fig. 1 presents the mole fraction of primary species at different temperatures for air plasma and CO_2 plasma by on NASA chemical equilibrium calculation program (CEA) [26], with a small amount of copper injecting into the medium. The equilibrium composition of species for air plasma and CO_2 plasma are functioned by temperature and pressure, and then the atomic oxygen concentration can be defined as function $X_O(T,P)$. The function $X_O(T,P)$ can be further simplified as $X_O(T)$ since the reservoir pressures in the plasma torch are measured by the pressure transducer. Then the mole fraction of atomic copper concentration in formula (4) can be simplified as follows:

$$X_{Cu} = \frac{I_{Cu}}{I_O} \cdot f(T) \cdot X_O(T)$$
$$f(T) = \left(\frac{v_{0\_Cu}}{v_{0\_O}} \frac{A_{Cu}}{A_O} \frac{g_{u\_Cu}}{g_{u\_O}} \frac{Q_o}{Q_{Cu}} \exp\left(-\frac{E_{Cu} - E_O}{kT}\right)\right)^{-1} \quad (5)$$

Where the spectral parameter of the selected spectral line for atomic oxygen and atomic copper in function $f(T)$ is shown in Table 1. As shown in formula (5), the mole fraction of atomic copper concentration can be acquired by measurements of spectral integrated intensities of the selected lines for atomic oxygen and atomic copper and gas temperature in the reservoir of the plasma torch.

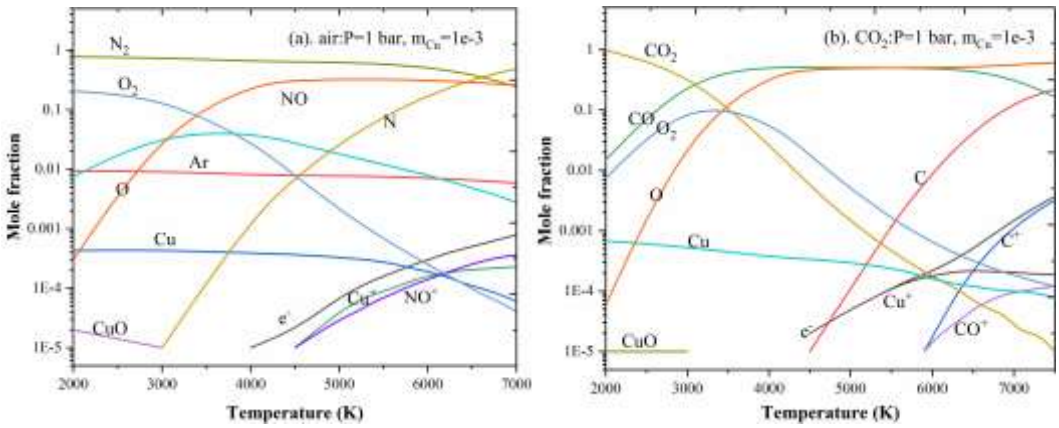

Fig. 1 Species composition at different temperatures by equilibrium calculation.

(a) air plasma;(b) CO_2 plasma

Fig. 2(a) and Fig. 2(b) show the ratio of copper-related mole fraction at different temperatures and pressures by equilibrium calculation for air plasma and CO_2 plasma, respectively. It can be seen that the copper element is mainly in the form of atomic copper and a very small amount of copper oxide at temperatures lower than 4000K, then the copper element ionizes with increasing temperature. The ratio of atomic copper decreases and the ratio of copper ions increases as the temperature increases, while the existence of copper oxide can be ignored at temperatures higher than 4000K. Thus, the erosion mass rate of cathode g [kg/s] can be can be expressed as formula (6), where t_1 and t_2 represent the moments when the test starts and ends respectively, x_{Cu} is atomic copper concentration by mass, R_{Cu} is the ratio of atomic copper, G is the mass flow rate of test medium. In this paper, optical diagnosis is installed at downstream of anode and the measured copper concentration by OES method is contributed by cathode erosion and anode erosion. The

erosion in the anode is negligible with erosion rate lower than 10^{-10}kg/C under the operation conditions in this paper almost without mass loss after tens of thousands of seconds of test by weighing method. Thus, the measured results of copper concentration by OES method can be considered as erosion in the cathode.

$$g = \frac{1}{t_2 - t_1} \cdot \int_{t_1}^{t_2} \frac{x_{Cu}}{R_{Cu}} \cdot G \cdot dt \qquad (6)$$

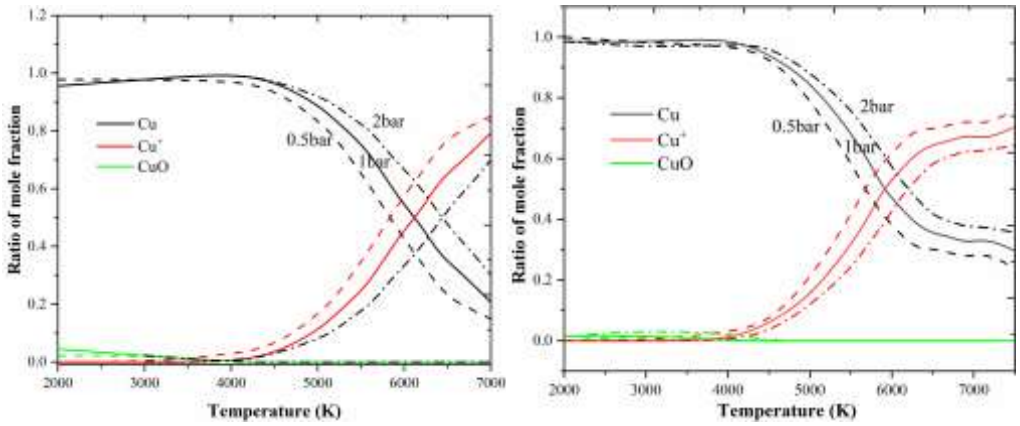

Fig. 2 Ratio of copper-related mole fraction at different temperatures and pressures by equilibrium calculation. (a) air plasma;(b) CO_2 plasma

For spectral intensity determination, a spectrometer is applied to monitor the emission spectrum for the selected lines for atomic copper and atomic oxygen. In this paper, seven line transitions at 510.6nm ($^2D^0_{5/2} \leftarrow {}^2P^0_{3/2}$),515.3nm ($^2P^0_{1/2} \leftarrow {}^2D_{3/2}$),521.8nm ($^2P^0_{3/2} \leftarrow {}^2D_{5/2}$), 522nm ($^2P^0_{3/2} \leftarrow {}^2D_{3/2}$) , 578.2nm ($^2D_{3/2} \leftarrow {}^2P^0_{1/2}$),793.3nm ($^2P^0_{1/2} \leftarrow {}^2S_{1/2}$) and 809.3nm ($^2P^0_{3/2} \leftarrow {}^2S_{1/2}$) for Cu I and three line transitions at 777.2 nm ($^5S^0_2 \leftarrow {}^5P_3$),777.4 nm ($^5S^0_2 \leftarrow {}^5P_2$) and 777.5 nm ($^5S^0_2 \leftarrow {}^5P_1$) for O I in the visible band are selected to monitor the atomic species and the fundamental spectroscopic data for the selected lines are presented in Table 1. As shown in Table 1, the two lines near 521.8 nm and 522 nm for Cu I and the three triplet lines near 777.2 nm,777.4 nm and 777.5 nm for O I can be processed by multi-peak Voigt fitting as shown in Fig. 3 and are considered as combined lines respectively owing to identical Einstein coefficient and excited state energy of upper energy state.

Table 1 Fundamental spectroscopic data for the selected atomic transitions [25]

Species	Selected lines	λ_0 (nm)	A_{ul} ($10^6 s^{-1}$)	E_l (cm^{-1})	E_u (cm^{-1})	g_l	g_u
O I	1	777.2	36.9	73768	86631	5	7

	(combined)	777.4	36.9	73768	86631	5	5
		777.5	36.9	73768	86631	5	3
Cu I	1	510.6	2.0	11202	30783	6	4
	2	515.3	60.0	30535	49935	2	4
	3	521.8	75.0	30783	49942	4	6
	(combined)	522.0	15.0	30783	49935	4	4
	4	578.2	1.65	13245	30535	4	5
	5	793.3	22.5	30535	43137	2	2
	6	809.3	45.9	30784	43137	4	2

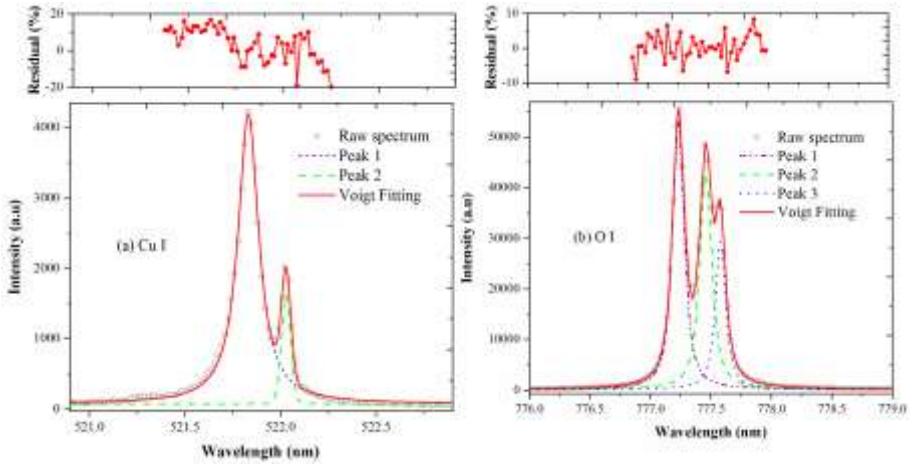

Fig. 3 Data processing of atomic spectrum. （a）Cu I；（b）O I.

The Boltzmann plot method is utilized to determine the gas temperature of the arc plasma under LTE conditions[27, 28]. The six selected atomic copper lines have a maximum upper energy difference of nearly 2.5eV as shown in Table 1 and the multi-line Boltzmann plot for atomic copper can obtain efficient measurements of excitation temperature downstream of anode. The relationship can be expressed as logarithm in both sides of formula (1) as shown in follows:

$$log(\frac{I\lambda}{g_u A_{ul}}) = -\frac{1}{kT} E_u + C \qquad (7)$$

Where the linear-fitting slope between $\ln(\frac{I\lambda}{g_u A_{ul}})$ in the vertical axis and E_u in the horizontal axis represents the reverse of excitation temperature and C is a constant. Fig. 4(a) time-resolved results of the spectral integrated intensities of the atomic copper lines under a typical test

condition and excitation temperature at one moment is determined by linear fitting as shown in Fig. 4 (b). The minor differences between the raw data and the linear fitting demonstrate the arc plasma investigating in this paper is in local thermal equilibrium.

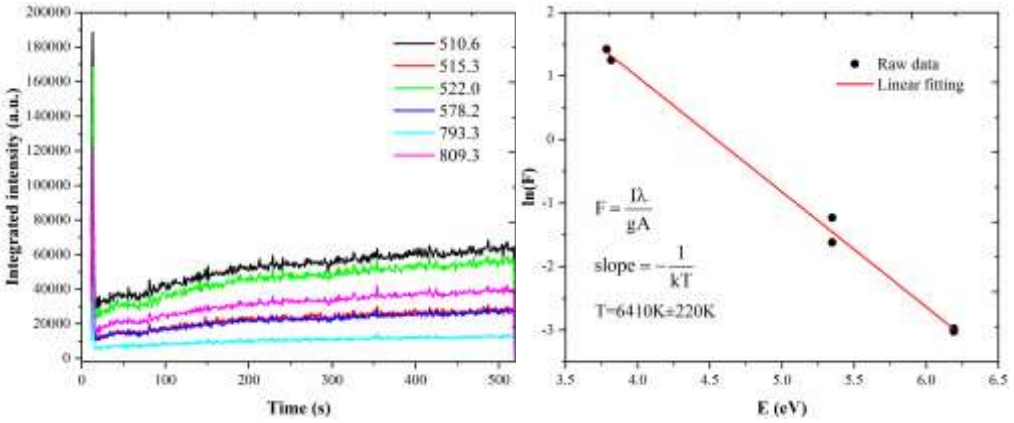

Fig. 4 Measured spectral intensity and temperature determination. (a) Time history of spectral intensities for Cu I;(b) Boltzmann plot for selected Cu I lines

3. Experimental Setup

The experiments are carried out in the high enthalpy arc-heated wind tunnel of China Academy of Aerospace Aerodynamics(CAAA). Fig. 5 shows the experimental setup of the arc-heated facility and optical system. The arc-heated facility is composed of a 300kW DC plasma torch, convergent-divergent conical nozzle, test cabin, vacuum system and associates. The plasma torch is ignited by a high-frequency power source for argon medium and operated by a DC power source for test medium, respectively. The electrodes of the plasma torch are manufactured by copper with water cooling and electrically insulated by the gas chamber installing between the electrodes. The test medium is injected tangentially into the chamber and the magnetic field generating by the excitation current in the coils drives the arc root to rotate on the cathode to reduce the cathode erosion. The test medium is heated by the arc and the high temperature gas medium is ejected from the nozzle and accelerated to supersonic flow to simulate the atmosphere aerothermal environment and interact with test model for thermal protection system (TPS) evaluation. In this paper, air and carbon dioxide are utilized to simulate the earth and Martian atmosphere, respectively.

For optical measurement, a quartz optical window is installed upstream of the cathode, with cold gas injecting close to the inner wall of the optical window, so as to protect the optical window from the high-temperature arc plasma. Meanwhile, an optical disk is installed between the anode and conical nozzle so as to acquire thermal radiation of the high-temperature flow in the reservoir

downstream of the anode. A schematic diagram of the optical disk is shown on the top section of Fig. 5. A hole is inserted into the inside cross-section for optical access and a quartz window with 4 mm diameter is mounted to collect the thermal radiation of arc plasma. For spectral measurement, an optical system with lens and slit combination collects gas radiation in the cathode region, while the gas radiation downstream of anode is measured through the optical disk. The collected radiation is passing through by multi-mode fibers and spectrally resolved by spectrometers with a maximum wavelength resolution of 0.02 nm over the spectral response range of 200-1000nm. For further data analysis, the spectral response of the optical system is calibrated by utilizing a NIST traceable tungsten halogen lamp (model 63355, Oriel Instruments). Besides, a high-speed CCD (HPC) camera is placed opposite the cathode to record the arc images inside the plasma torch and the arc column characteristics are captured under different magnetic fields.

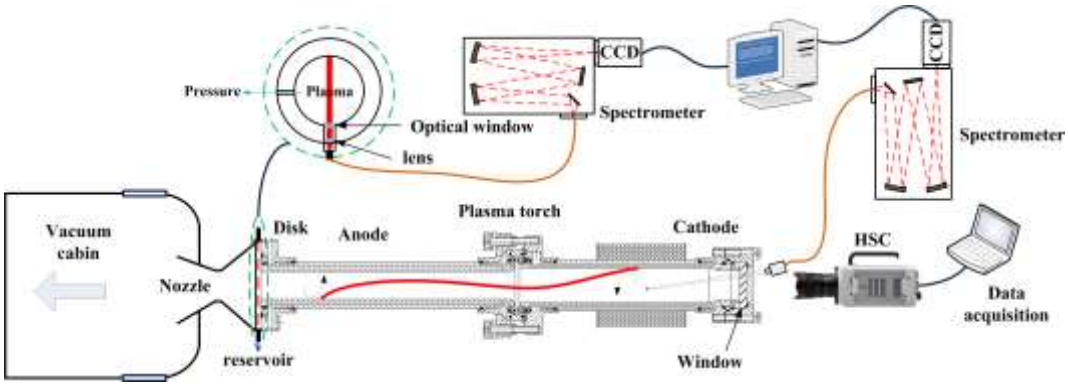

Fig. 5 Schematic of the experimental setup of the arc-heated facility and optical systems.

4. Results and discussions

4.1 Spectroscopic characteristics

Fig. 6 and Fig. 7 show typical raw emission spectrums positioned at cathode and reservoir downstream of anode for air plasma and CO_2 plasma, respectively. The emission spectrum for air plasma is mainly composed of isolated atomic line of O I, N I ,Cu I and Fe I in the region of cathode and reservoir downstream of anode, which Cu I and Fe I come from the erosion of electrodes and associates of plasma torch, respectively. There exists very weak continuum radiation in the ultraviolet-visible band indicating fully dissociation of air under this condition. It can been seen from Fig. 6 (a) and Fig. 6 (b) that there shows difference for emission radiation at cathode and reservoir downstream of anode. In the region of cathode, more atomic lines of Fe I are excited, N_2

first positive spectrum can be observed in the spectral range of 600-700nm, and the ratio of atomic nitrogen lines compared to atomic oxygen is larger than the values in the reservoir downstream of anode, because the gas temperature in the cathode is higher than that of reservoir downstream of anode leading to more complete dissociation and ionization. The emission spectrums for CO_2 plasma are different from the results for air plasma, while there exist strong atomic line of C I in the ultraviolet band and C_2 Swan continuum radiation in the spectral range of 400-600nm. It can be observed that stronger atomic lines of Fe I and the ratio of spectral lines near 926nm versus spectral lines near 777nm for atomic oxygen indicates higher temperature in the cathode compared with that in the reservoir downstream of anode for CO_2 plasma, which are in consistence with that for air plasma.

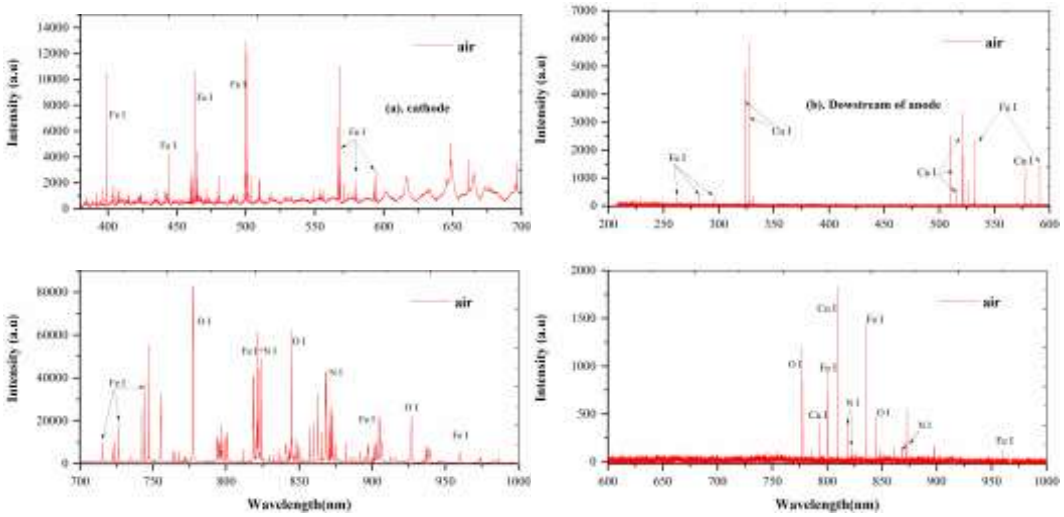

(a) Cathode **(b) Reservoir downstream of anode**

Fig. 6 Raw spectrum positioned at cathode and reservoir downstream of anode for air plasma

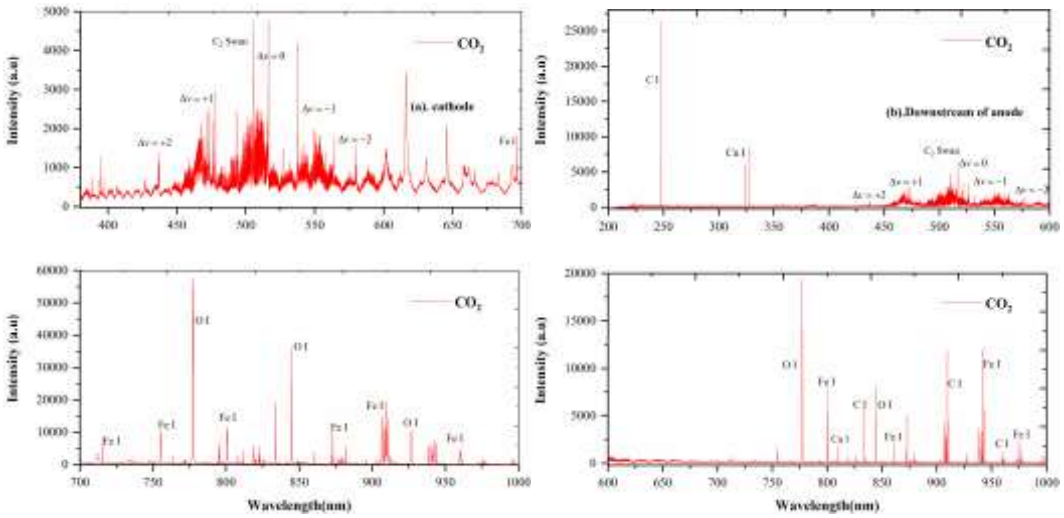

(a) Cathode **(b) Reservoir downstream of anode**

Fig. 7 Raw spectrum positioned at cathode and reservoir downstream of anode for CO_2 plasma

Fig. 8(a) shows the spectral integrated intensities of atomic oxygen near 777nm for air plasma and CO_2 plasma under different operation current and a fixed mass flowrate of 7 g/s. It is obvious that the spectral intensity of atomic oxygen is exponentially increasing as the operation current increases, indicating increasing gas temperature of the arc plasmas. The exponential growth of spectral intensity is consistent with the formula (2) by a Maxwell-Boltzmann distribution. Fig. 8(b) investigates the effect of mass flowrate on the spectral intensity for air plasma. The spectral intensities of atomic oxygen firstly increase when the mass flowrate increases from 7 g/s to 10 g/s, then decrease when the mass flowrate increases to 13g/s at the three operation currents, indicating temperature decrease of arc plasma at high mass flowrate.

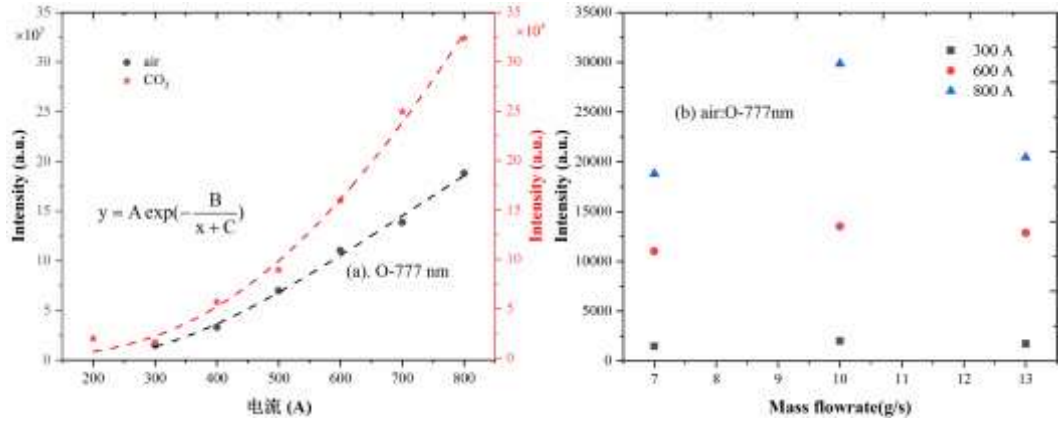

Fig. 8 Spectral intensity of atomic oxygen near 777nm. (a) under different operation current;(b) under different mass flowrate.

4.2 Temperature measurements

Fig. 9(a) and Fig. 9(b) show time-resolved gas temperatures for air plasma at different operation currents and magnetic fields, respectively. The gas temperatures can maintain stable over the operation time at high operation currents and are seriously fluctuated at operation currents of 350A, indicating that the arc can operate in stable condition at operation currents high than critical threshold. As shown in Fig. 9(b), the time-resolved gas temperatures for air plasma are stable at the three magnetic fields. Fig. 9(c) and Fig. 9(d) give the statistic results of average temperature at different operation currents and magnetic fields, respectively. The average value of gas temperature shows an increasing tendency as the operation current increases, which is in consistency with the change of chamber pressure. Moreover, the rate of gas temperature and pressure are decreasing as the operation current increases, illustrating that the enthalpy of arc plasma cannot always become higher with increasing operation current. It is interested that the gas temperature is weak negative related to the magnetic field at the operation currents of 600A and 950A. The reason is that the arc column is gradually approach to the inner wall surface of the electrodes as the magnetic field increases, leading to more severe wall heating for the electrodes and lower thermal efficiency for the plasma torch.

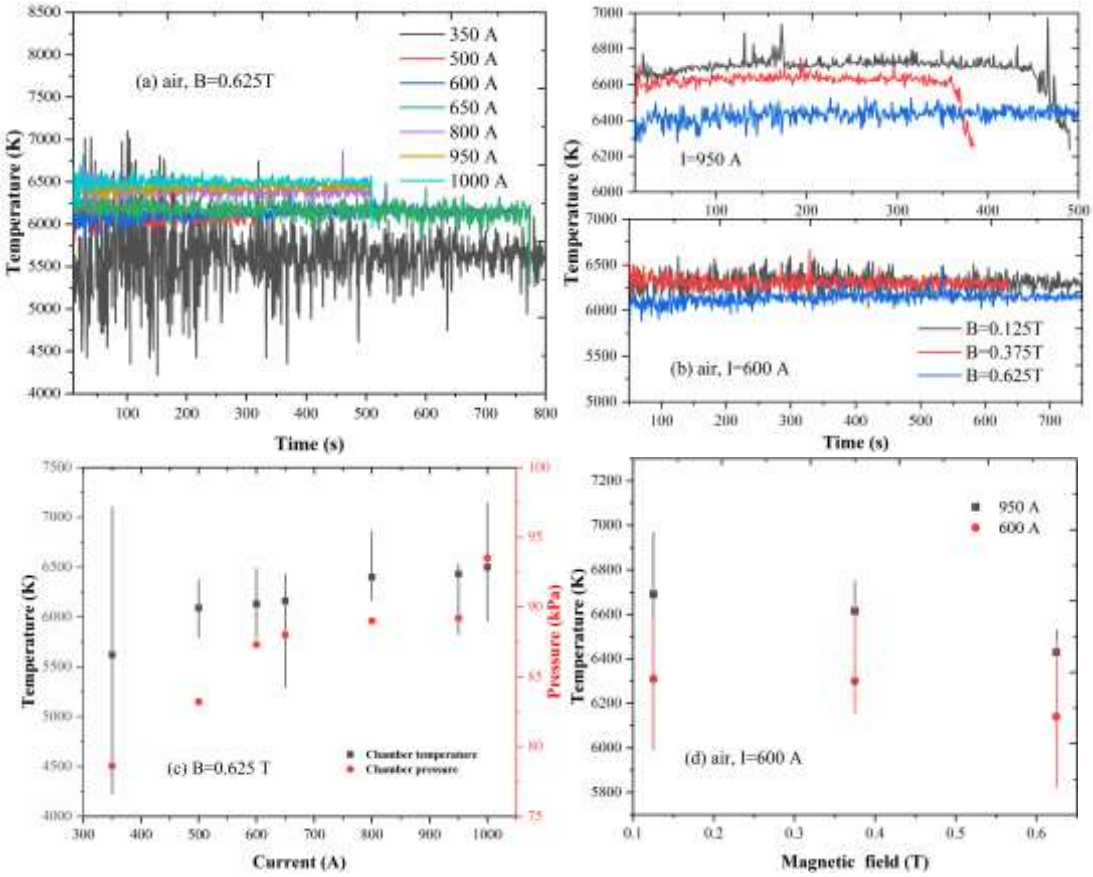

Fig. 9 Measured temperature for air plasma. (a) different current; (b) different magnetic field; (c) average temperature under different current; (d) average temperature under different magnetic field

Fig. 10(a) shows the measured results of gas temperature for CO_2 plasma at different operation currents and a fixed magnetic field of 0.125T. The gas temperatures are less fluctuated with increasing operation current, which agrees with the results for air plasma. The time-resolved gas temperature is stable under different magnetic fields for CO_2 plasma as shown in Fig. 10(b). the average temperatures for CO_2 plasma are increasing with increasing operation current and show a slightly decrease with the increase of magnetic field, which are in accordance with the evolution for air plasma as shown in Fig. 9.

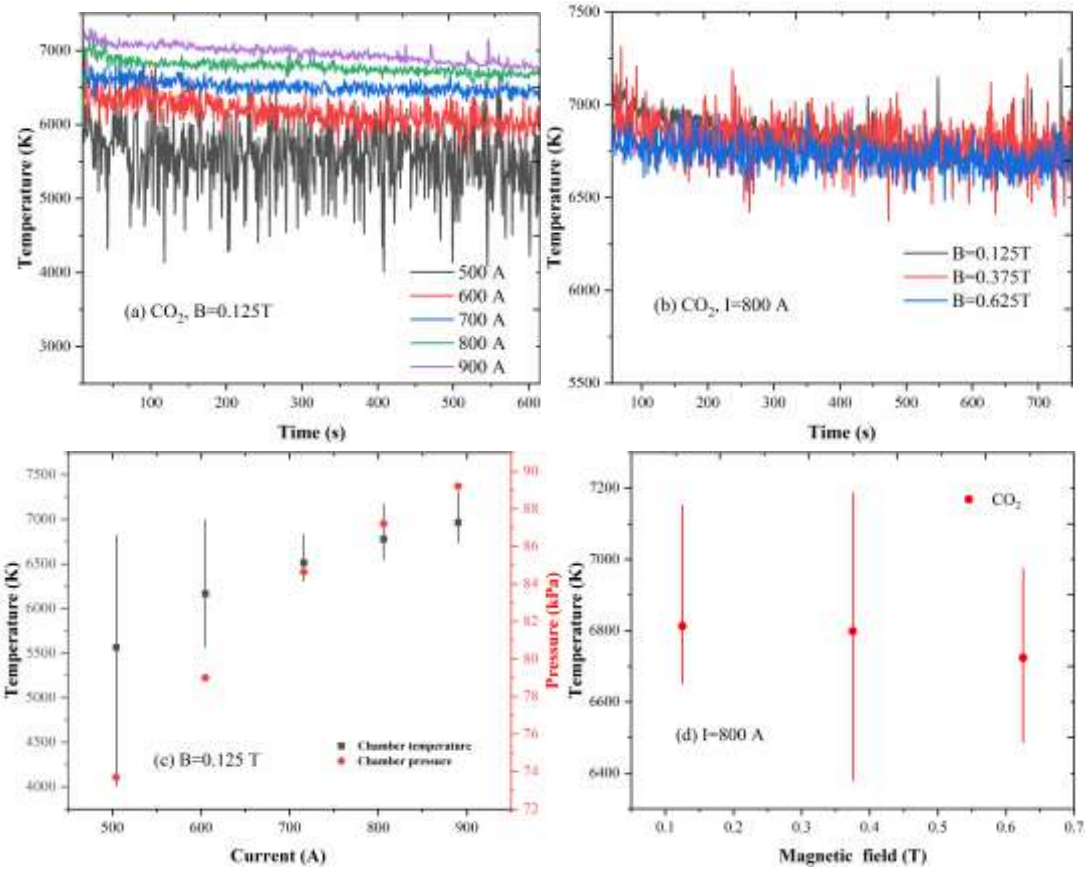

Fig. 10 Measured temperature for CO_2 plasma. (a) different current; (b) different magnetic field; (c) average temperature under different current; (d) average temperature under different magnetic field

4.3 Electrode erosion

Fig. 11(a) shows measured atomic copper concentration by mole for 500s continuous operation of the plasma torch by utilizing the six selected copper lines. The measured atomic copper concentrations by the six lines keep in good consistency. As the arc is ignited, the mole fraction of atomic copper quickly increases and reaches to a peak within 1-2 s as shown in the partial enlargement of Fig. 11(a). Then, the atomic copper concentration returns to a lower level and slowly increases during the arc long-time operation. The peak of copper concentration in the early ignition stage is attributed to the reason that arc spots on the electrodes are unstable and arc column is partially established during arc initiation. It can be observed that there exists another peak of copper concentration at the moment of 470 s, indicating aggravated electrode erosion owing to uneven surface condition of the cathode. The measured values of copper concentration by the six lines show a litter difference owing to different temperature sensitivity and spectral response of the line transitions. The average values of atomic copper concentration during the whole operation time are given in Fig. 11(b). the average values of atomic copper concentration

are 92.6 ppm and 58.6 ppm by mole under the two cases and the maximum deviation of the copper concentrations by the six lines is 40% compared to the average value, which are considered as a contribution of measurement uncertainty of atomic copper concentration in the following section. It can be observed that the measure result by atomic copper line near 522nm is closest to the average value and measurements by this line can be represented to evaluate the cathode erosion rate owing to its highest intensity of $g_u A_{ul}$ and excited state energy for upper energy state as shown in Table 1. Thus, the spectral measurement can obtain highest signal-to-noise ratio(SNR) signal and lowest temperature sensitivity so as to enabling more accurate measurements of copper concentration.

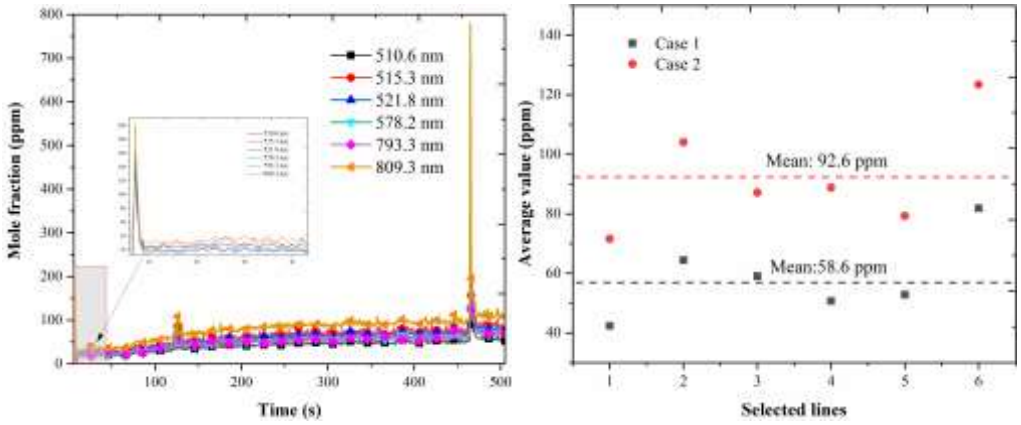

Fig. 11 Measured atomic copper concentration by mole. (a) time-resolved results;(b) average values for selected lines.

Fig. 12(a) and Fig. 12(b) show the measured mass rate of cathode erosion by the OES and weighing method for air plasma and CO_2 plasma, respectively. The uncorrected results by OES method represent measurements only considering contribution of atomic copper, while the corrected results by OES method represent measurements considering contribution of atomic copper and copper ions as shown in Fig. 2 and are in good accordance with the results by weighing method. The mass rates of cathode erosion increase with increasing operation currents for air plasma and CO_2 plasma. The differences between the OES measurements and weighing measurement are larger at lower operation currents and become larger at higher operation currents, because the measurements by the OES method are more accurate with smaller measurement uncertainty at higher temperature. It is interested that the mass rate of electrode erosion for air plasma decrease to a lower level at operation currents of 1000A by the OES and weighing

measurements with repeated experiments verification as shown in the dashed box of Fig. 12(a) and the reason is attribute to splitting of arc root leading to decrease of current density.

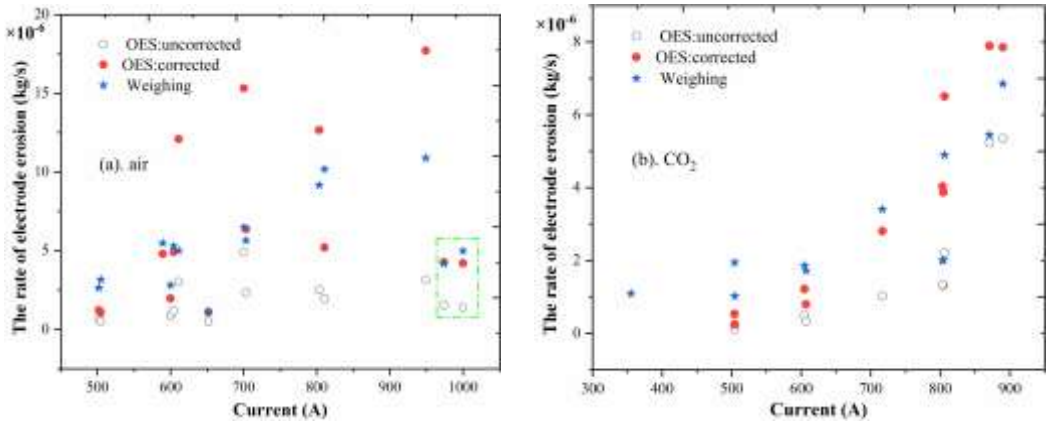

Fig. 12 Comparison of the cathode erosion mass rate by OES and weighing method.

(a)air; (b) CO_2

Fig. 13(a) and Fig. 13(b) show the cathode erosion rate by weighing method under different operation current and magnetic field for air plasma and CO_2 plasma, respectively. The cathode erosion rates ranges between 2×10^{-9} kg/C to 1.3×10^{-8} kg/C for air plasma and between 5×10^{-10} kg/C to 9×10^{-9} kg/C for CO_2 plasma over the operation range, indicating lower cathode erosion for CO_2 plasma. The reason is that the size of arc root for air plasma is smaller than that for CO_2 plasma as shown in the photographs of cathode after test of Fig. 15 leading to larger current density and serious electrode erosion, and the existence of carbon element protecting the inner surface of electrodes from erosion and the mechanism is discussed by SEM images in the following section. Moreover, the influence of operation current and magnetic field on the cathode erosion rate show difference for air plasma and CO_2 plasma. The cathode erosion rate is positive related to the operation current and magnetic field over the operation range for air plasma, while the cathode erosion rate for CO_2 plasma is positive related to the operation current at low magnetic field of 0.125 T and maintain stable at a lower level of 3×10^{-9} kg/C at high magnetic fields of 0.375 T and 0.625T over the operation current range. The reason for this difference is that the arc column for air plasma is closely approaching to the inner wall surface of the cathode with increasing magnetic field leading to more severe wall heating for the cathode and electrode erosion, while this tendency is not so obvious for CO_2 plasma as shown in the arc images captured for air plasma and CO_2 plasma of Fig. 14. Besides, the carbon element covering in the inner surface of the electrode provides better protection for the cathode. Thus, it is not beneficial for reduction of cathode erosion

rate with higher magnetic field within 0.125-0.625T for air plasma, while higher magnetic field ensures cathode erosion rate at low levels for CO_2 plasma.

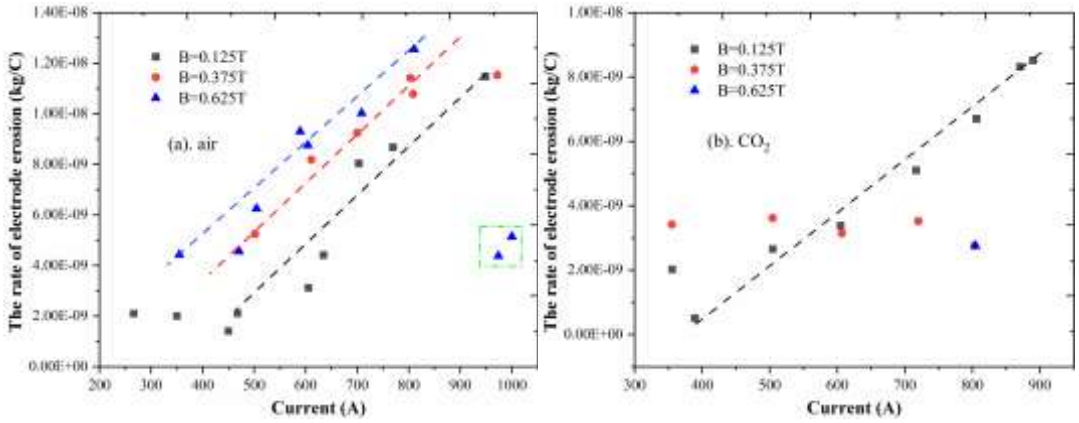

(a) air (b) CO_2

Fig. 13 Comparison of the cathode erosion rate for air plasma and CO_2 plasma under different operation current and magnetic field

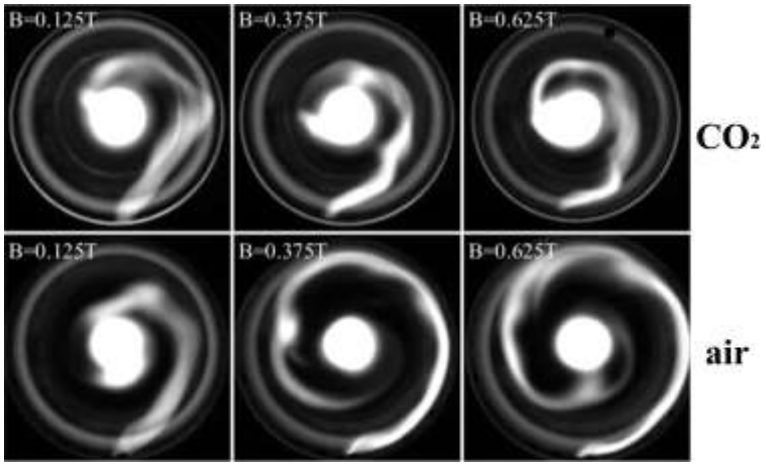

Fig. 14 Comparison of arc images captured for air plasma and CO_2 plasma under different magnetic field. I=300A

Fig. 15 Photographs of cathode after test for air plasma and CO_2 plasma.

Fig. 15 gives the photographs of cathode after test for air plasma and CO_2 plasma. It is obvious that the surface of the cathode is covered with a large amount of black substance which should be copper oxides or carbide and the covering area and size of black substance is significantly larger than that for air plasma. Fig. 16 shows the surface morphology of the cathode where electrode erosion is presented under different test media of air and CO_2,respectively. The industrial copper material is a polycrystalline material containing grains of different sizes and shapes and various impurities. The impurities gradually evaporate and form vacuoles and cracks when the arc is in operation and the inner surface of cathode is heated to high temperature. The atomic oxygen and carbon in the arc plasma penetrate into the crystal lattice of copper through the cracks and form copper oxides or carbide. The cathode surface forms a structure with characteristics of melting and resolidification for air plasma and the scale of the equiaxed structure is about 500 μm as shown in Fig. 16(a). Compared with surface structure of cathode for air plasma, the melting surface of cathode for CO_2 plasma presents a more complex secondary structure with smaller arc spots and the size of the melting feature increases to about 700 μm. Besides, it is obvious that the groove-like cracks can be observed between the structural units, while most of the cracks have been filled into a relatively flat surface compare to the surface morphology of cathode for air plasma.

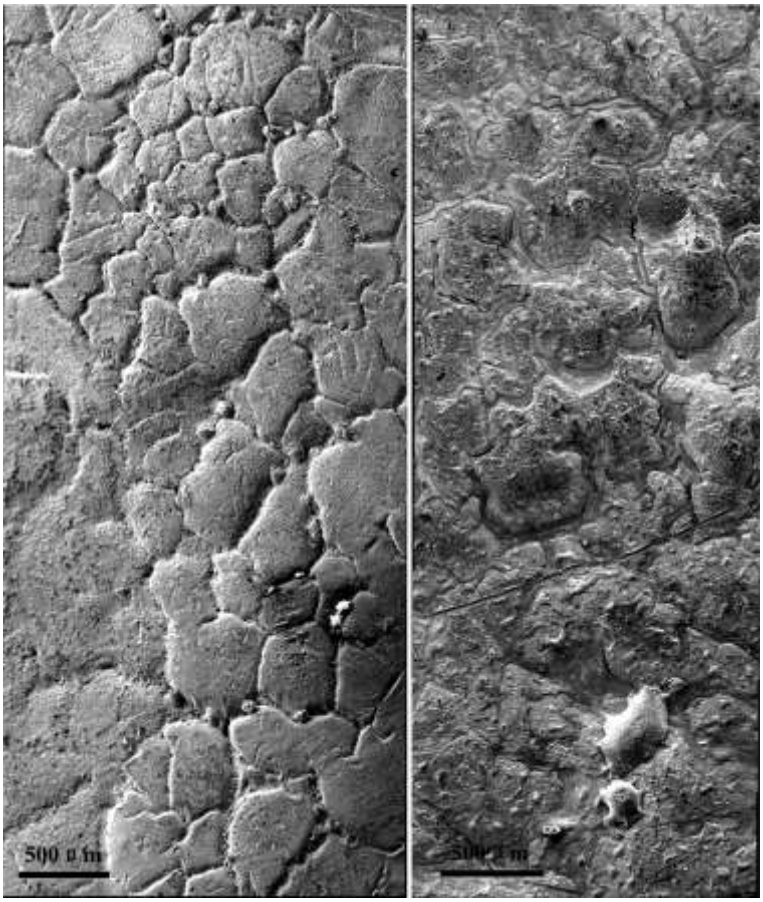

Fig. 16 Surface morphology of cathode for air and CO_2 operation.(a) air;(b) CO_2

Fig. 17 and Fig. 18 show a local surface morphology and SEM image of the cathode erosion area for air plasma and CO_2 plasma, respectively. The elements of the melting and resolidification zone for air plasma are constituent by atomic copper and atomic oxygen and the concentration distributions for the two species are in great consistency, indicating there exist a molten liquid layer of copper on the cathode surface causing by the force heat exchange and certain degree of oxidation under the operation of high enthalpy air plasma. As shown in in the SEM images of Fig. 18, atomic copper, oxygen and carbon exist simultaneously in the melting and resolidification region of cathode erosion for CO_2 plasma, indicating simultaneous processes of melting, oxidation and C diffusion on the surface of cathode. The distributions of species concentration show the atomic oxygen concentration is higher in the groove-shaped area and the carbon concentration is higher in the central structured area, demonstrating more significant oxidation in the groove-shaped area and more obvious diffusion of carbon element in the central structured area.

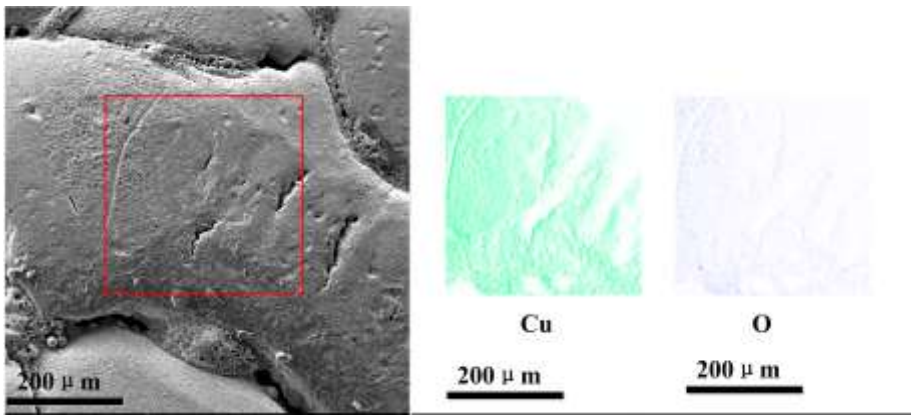

Fig. 17 Typical surface morphology and SEM image of cathode for air operation. (a) surface morphology; (b) distribution: Cu;(c) distribution: O

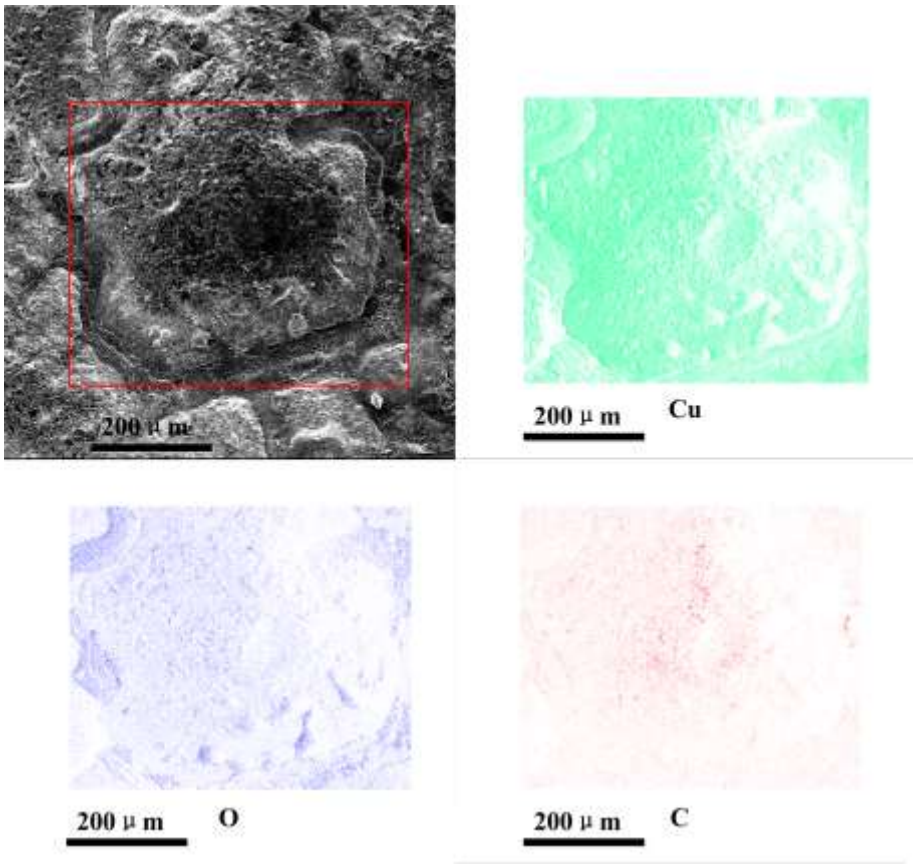

Fig. 18 Typical surface morphology and SEM image of cathode for CO_2 operation. (a) surface morphology; (b)distribution: Cu; (c) distribution:O; (d) distribution:C

In order to confirm the diffusion behavior of carbon element in the cathode melting area for CO_2 plasma, the morphology in the cross-section of the melting area are presented and the concentration distribution along the black-white dashed line are shown in Fig. 19. Two elements of copper and carbon are detected indicating that the element of oxygen do not diffuse to the inner area of cathode and only exists on the surface of cathode. Moreover, the distribution of carbon as

shown in Fig. 19(b) indicates that the depth of carbon diffusion in the molten area is about 5μm and the sharp peak of carbon concentration is attributed to difference in the secondary electron contrast of the microstructure in the region with a higher concentration of carbon element. Fig. 19(c) shows the SEM images in the cross-section of the melting area. It must be note that there is no effective information of element concentration in the southeast area of the images due to the difference in surface height. The spatial distribution of copper element is uniform in the whole area, while higher concentration of carbon element is distributed in the southwest area "A" which is adjacent to the inner surface of cathode verifying the diffusion paths of carbon element from the surface to the interior in the cross section. The diffusing area for carbon element can be represented by the area below the read dashed line in Fig. 19 (a). Thus, the distribution of carbon elements is beneficial for reduction of cathode erosion owing to its higher melting temperature and blockage effect to prevent rapid oxidation inside the cathode.

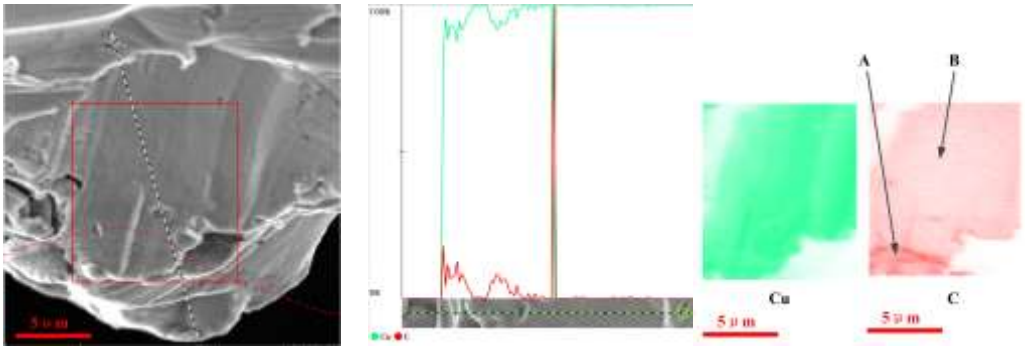

Fig. 19 Typical surface morphology of the cross section of electrode molten region and SEM image of cathode for CO_2 operation. (a) surface morphology; (b) species distribution: Cu, C;(c) surface distribution: : Cu, C

4.4 Sensitivity and uncertainty analysis

For measurement uncertainty evaluation for the OES method, the experimental uncertainty of the cathode erosion stems from associated uncertainty in the four error sources, as shown in the formula (5) to formula (7):

(1) measurement uncertainty of spectral integrated intensity for Cu I, deriving from the maximum residuals of Voigt fitting processing, the uncertainty is 20% for the selected combined line near 522nm in Table 2;

(2) measurement uncertainty of spectral integrated intensity for O I, deriving from the maximum residuals of Voigt fitting processing, the uncertainty is 10% for the selected triplet line of atomic oxygen;

(3) measurement deviation of the selected six lines for Cu I. since the atomic copper concentration are represented by the measurements of copper line near 522.0nm. the difference between the six selected lines must be considered and the maximum difference is 40% for the six lines as shown in Fig. 11(b);

(4) uncertainty of $R_{Cu}(T)$; the ratio of atomic copper $R_{Cu}(T)$ is a function of temperature as shown in Fig. 2

(5) uncertainty of $f(T)$;

(6) uncertainty of $X_O(T)$

The uncertainties determination of $R_{Cu}(T)$, $f(T)$ and $X_O(T)$ stems from the uncertainty of gas temperature T, and the uncertainty of gas temperature can be obtained from the linear fitting process of multi-line Boltzmann plot as shown in Fig. 4(b) and the uncertainty of gas temperature is 3%-4% over the temperature range of 5500K-7000K, which there exists smaller error at higher temperature. Based on equilibrium calculation, the Fig. 20(a) and Fig. 20(b) give the sensitivity analysis for $X_O(T)$ for test medium of air and CO_2, respectively. The uncertainty of $X_O(T)$ is 1.2 %-4.4% for air plasma is 0.4%-3.5% for CO_2 plasma over the temperature of 5500K-7000K. Meanwhile, the sensitivities of $f_i(T)$ for the selected six lines and $R_{Cu}(T)$ are presented in Fig. 21. It can be seen that the sensitivity $(df/f)/(dT/T)$ for the spectral lines near 515.3nm and 522.0nm are smaller than that for the other four lines because of higher excited state energy for upper energy state E_u. The sensitivity $(df/f)/(dT/T)$ for spectral line near 522.0nm is 8-12 and the uncertainty of $f(T)$ is 24%-48% over the temperature range of 5500K-7000K. The sensitivity $(dR/R)/(dT/T)$ is 3.1-8.8 for air plasma and 0.5-4.5 for CO_2 plasma, leading to measurement uncertainty of 12.4%-26.4% for air plasma and 1.5%-18% for CO_2 plasma over the temperature range of 5500K-7000K.

The total uncertainties of the OES method for cathode erosion rate measurements are 58.2%-67.5% for air plasma and 51.9%-68.7% for CO_2 plasma over the temperature range of 5500K-7000K, respectively. All the information are illustrated in Table 2. The measurement

accuracy by the OES method is sufficient to evaluate the cathode erosion rate allowing half magnitude measurement error in previous work[12, 29].

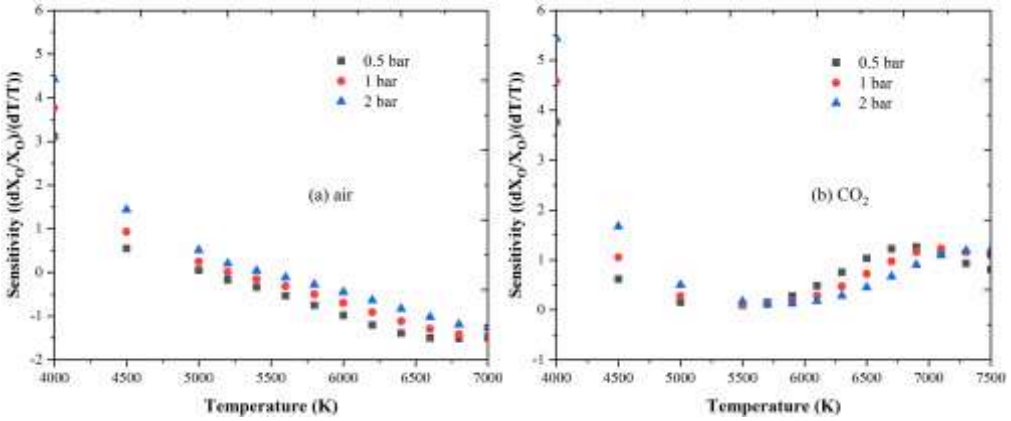

Fig. 20 Sensitivity analysis for $X_O(T)$.(a) air;(b) CO_2.

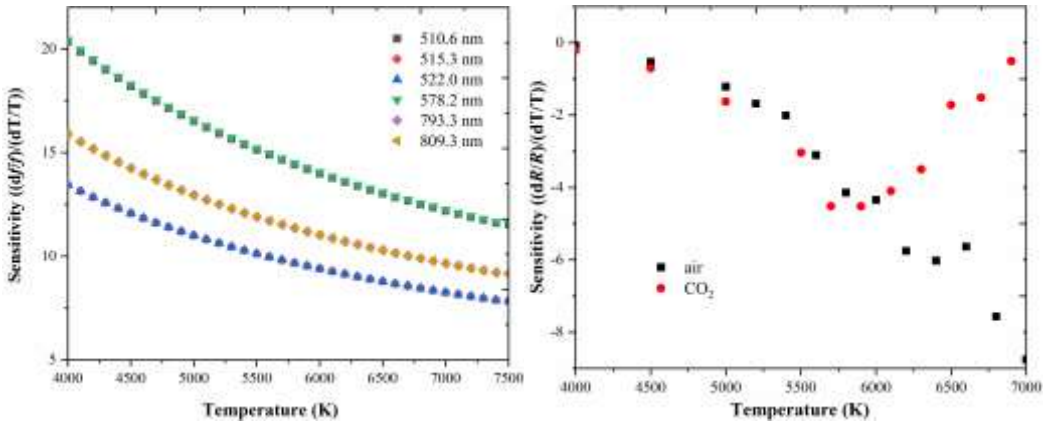

Fig. 21 Sensitivity analysis for $f_i(T)$ and $R(T)$. (a) $f_i(T)$, i=1-6;(b) $R_{Cu}(T)$.

Table 2 Evaluation of uncertainty for cathode erosion rate measurements

Test medium	I_{Cu}	I_O	different lines	$X_O(T)$	$f(T)$	$R_{Cu}(T)$	Total uncertainty
air	20%	10%	40%	1.2 %- 4.4%	24%-48%	17.2%-26.4%	58.2%-67.5%
CO_2				0.4%-3.5%		2%-18%	51.9%-68.7%

5. Conclusion

In this paper, *in-situ* quantitative measurements are performed in a 300 kW DC magnetically-rotating linear plasma torch of CAAA to investigate thermal characteristics of arc plasma and electrode erosion by utilizing optical emission spectroscopy. Spectral characteristics of the high-temperature plasma in the water-cooling copper cathode and reservoir downstream of anode are carried out for simulation of earth atmosphere and Martian atmosphere by the selected six line transitions of Cu I in the visible band of 510-810 nm and the triplet lines of O I near 777 nm.

Time-resolved gas temperatures and mole fraction of copper concentrations are measured to evaluate the state of arc plasma and cathode erosion at different operation currents and magnetic fields. The average temperatures are strong positive related to the increasing operation current and are weak negative related to the magnetic field for air plasma and CO_2 plasma. The erosion mass rates of the cathode by the OES method are in good accordance with the measurements by traditional weighing method over the operation range, demonstrating validity and accuracy for the developed OES method. The erosion rates of cathode for air plasma range from 2×10^{-9} kg/C 1.3×10^{-8} kg/C within operation currents of 250A-950A and increase with increasing magnetic field over the range of 0.125T-0.625T. The decrease of erosion rates of cathode have be found at operation current of 1000A attributing to arc root splitting leading to decrease of current density.

The erosion rates of cathode for CO_2 plasma are lower than that for air plasma and are strongly positive related to the operation currents at magnetic field of 0.125T and maintain stable at higher magnetic field of 0.375T-0.625T. It is not beneficial for reduction of cathode erosion rate under higher magnetic field within 0.125-0.625T for air plasma, while higher magnetic field ensures cathode erosion rate at low level for CO_2 plasma due to carbon deposition covering in the inner surface of the electrode by the SEM images. The SEM images verify the diffusion paths of carbon element from the surface to the interior in the cross section and the element of oxygen do not diffuse to the inner area of cathode preventing oxidation inside the cathode for CO_2 plasma. Detailed discussions of sensitivity and uncertainty by the OES method are given and the uncertainties of cathode erosion rate are 58.2%-67.5% for air plasma and 51.9%-68.7% for CO_2 plasma over the temperature range of 5500 K-7000 K, respectively. The developed OES method demonstrates great potential for real-time diagnosis for electrode erosion and thermal characteristics of arc plasma and provides quantitative data to assess the aerothermal environment for TPS evaluation.

Acknowledgments

This work was supported by the National Natural Science Foundation of China (grant numbers 11802299) and Young Elite Scientists Sponsorship Program by CAST.

References

[1] A. Calomino, W. Bruce, P. Gage, D. Horn, M. Mastaler, D. Rigali, J. Robey, L. Voss, J. Wahlberg, C. Williams, Evaluation of the NASA Arc Jet Capabilities to Support Mission Requirements, NASA/SP-2010-577

[2] Bugel M, Reynier P, Smith A. Review of European aerodynamics and aerothermodynamics capabilities for sample return missions[C]//Proceedings of the 6th European symposium on aerodynamics for space vehicles. 2008.

[3] F.K. Lu, Advanced hypersonic test facilities[M], AIAA2002.

[4] Marotta A, Sharakhovsky L I. A theoretical and experimental investigation of copper electrode erosion in electric arc heaters: I. The thermophysical model[J]. Journal of Physics D: Applied Physics, 1996, 29(9): 2395.

[5] MacDermott W, Horn D, Fisher C. Flow contamination and flow quality in arc heaters used for hypersonic testing[C]//17th Aerospace Ground Testing Conference. 1992: 4028.

[6] Smith R K, Cunningham J, Wagner D A. High Enthalpy Material Test Facility Design Improvements in Japan[M]. AIAA, 1994.

[7] Mitsuda M, Oda T, Tagashira S, et al. On the characteristics of a plasma arc heater for a high enthalpy wind tunnel[C]//32nd Thermophysics Conference. 1997: 2494.

[8] Menart J, Lin L. Numerical study of a free-burning argon arc with copper contamination from the anode[J]. Plasma chemistry and plasma processing, 1999, 19(2): 153-170.

[9] S. Kim, Development of tunable diode laser absorption sensors for a large-scale arc-heated-plasma wind tunnel[D], Stanford University, 2004.

[10] Luo L, Wang Y, Liu L, et al. Ablation behavior of C/SiC composites in plasma wind tunnel[J]. Carbon, 2016, 103: 73-83.

[11] Guile A E. Erosion of non-refractory cathodes in arc plasma devices[C]//Proc. 4th Int. Symp. on plasma Chem., Zurich. 1979.

[12] Thermal plasma torches: design, characteristics, application[M]. Cambridge Int Science Publishing, 2007.

[13] Bolshov M A, Kuritsyn Y A, Romanovskii Y V. Tunable diode laser spectroscopy as a technique for combustion diagnostics[J]. Spectrochimica Acta Part B: Atomic Spectroscopy, 2015, 106: 45-66.

[14] Hanson R K, Spearrin R M, Goldenstein C S. Spectroscopy and optical diagnostics for gases[M]. Switzerland: Springer, 2016.

[15] Wernitz R, Eichhorn C, Herdrich G, et al. Plasma wind tunnel investigation of european ablators in air using emission spectroscopy[C]//42nd AIAA Thermophysics Conference. 2011: 3761.

[16] Loehle S, Hermann T A, Zander F, et al. Echelle spectroscopy for high enthalpy flow diagnostics[C]//46th AIAA Thermophysics Conference. 2016: 3691.

[17] Hermann T, Löhle S, Zander F, et al. Characterization of a reentry plasma wind-tunnel flow with vacuum-ultraviolet to near-infrared spectroscopy[J]. Journal of Thermophysics and Heat Transfer, 2016, 30(3): 673-688.

[18] Lin X, Ou D B, Peng J L, et al. Cooling-Water Leakage Diagnosis Using Optical Emission Spectroscopy for a Large-Scale Arc-Heated Facility[J]. Journal of Thermophysics and Heat Transfer, 2019, 33(4): 900-906.

[19] Ochkin V N. Spectroscopy of low temperature plasma[M]. John Wiley & Sons, 2009.

[20] Kim S, Jeffries J, Hanson R, et al. Measurements of gas temperature in the arc-heater of a large scale arcjet facility using tunable diode laser absorption[C]//43rd AIAA aerospace sciences meeting and exhibit. 2005: 900.

[21] Nations Martin M, Chang L S, Jeffries J B, et al. Monitoring temperature in high enthalpy arc-heated plasma flows using tunable diode laser absorption spectroscopy[C]//44th AIAA Plasmadynamics and Lasers Conference. 2013: 2761.

[22] Park C. Evaluation of real-gas phenomena in high-enthalpy aerothermal test facilities: A review[J]. Journal of thermophysics and heat transfer, 1997, 11(3): 330-338.

[23] Cipullo A, Savino L, Marenna E, et al. Thermodynamic state investigation of the hypersonic air plasma flow produced by the arc-jet facility SCIROCCO[J]. Aerospace Science and Technology, 2012, 23(1): 358-362.

[24] Colonna G, Capitelli M. A few level approach for the electronic partition function of atomic systems[J]. Spectrochimica Acta Part B: Atomic Spectroscopy, 2009, 64(9): 863-873.

[25] A. Kramide, Ralchenko,Yu, NIST Atomic Spectra Database(ver.5.6.1)[online].Available: http://physics.nist,gov./asd[2019,June 10], National institute of Standards and Technology, Gaithersburg, 2018.

[26] McBride B J. Computer program for calculation of complex chemical equilibrium compositions and applications[M]. NASA Lewis Research Center, 1996.

[27] Ohno N, Razzak M A, Ukai H, et al. Validity of electron temperature measurement by using Boltzmann plot method in radio frequency inductive discharge in the atmospheric pressure range[J]. Plasma and fusion research, 2006, 1: 028-028.

[28] Griem H R. Principles of plasma spectroscopy[M]. 2005.

[29] Boulos M I, Fauchais P L, Pfender E. Handbook of thermal plasmas[M]. New York, NY, USA:: Springer International Publishing, 2019.